# Refinement of Transition-Edge Sensor Dimensions for the X-ray Integral Field Unit on ATHENA

N. A. Wakeham, J.S. Adams , S.R. Bandler, S. Beaumont, J.A. Chervenak, R.S. Cumbee, F.M Finkbeiner, J.Y. Ha, S. Hull, R.L. Kelley, C.A. Kilbourne, F.S. Porter, K. Sakai , S.J. Smith, E.J. Wassell, S. Yoon

*Abstract*— **At NASA Goddard Space Flight Center, we have previously demonstrated a kilo-pixel array of transition-edge sensor (TES) microcalorimeters capable of meeting the energy resolution requirements of the future X-ray Integral Field Unit (X-IFU) instrument that is being developed for the Advanced Telescope for High ENergy Astrophysics (ATHENA) observatory satellite. The TES design in this array was a square device with side length of 50 μm. Here, we describe studies of TES designs with small variations of the dimensions, exploring lengths, parallel to the current direction, ranging from 75 μm to 50 μm and widths, perpendicular to the current direction, ranging from 50 μm to 15 μm. We describe how these changes impact transition properties, thermal conductance and magnetic field sensitivity. In particular, we show that using a TES with a length of 50 μm and width of 30 μm may be a promising route to reduce the maximum time-derivative of the TES current in an X-ray pulse and reduce the sensitivity of the TES to magnetic field.**

*Index Terms*—**Superconducting devices, Superconducting photodetectors, Transition-edge sensor, X-ray microcalorimeter**

## I. INTRODUCTION

**T**HE X-ray Integral Field Unit (X-IFU) is an instrument on the Advanced Telescope for High ENergy Astrophysics (ATHENA), an ESA led X-ray observatory satellite due for launch in the 2030's [1]. X-IFU is currently baselined to have 2,376 transition-edge sensor (TES) microcalorimeter pixels in a single array read out using time division multiplexing (TDM)

N. A. Wakeham, J.S. Adams, and K. Sakai are with Center for Space Sciences and Technology, University of Maryland, Baltimore County, Baltimore, MD 21250 and NASA Goddard Space Flight Center (GSFC), Greenbelt, MD 20771, USA.

S. Beaumont is with Center for Space Sciences and Technology, University of Maryland, Baltimore County, Baltimore, MD 21250, IRAP, 9 Avenue du Colonel Roche, 31400 Toulouse, France, and NASA Goddard Space Flight Center (GSFC), Greenbelt, MD 20771, USA.

R.S. Cumbee is with University of Maryland, College Park, MD 20742 and NASA Goddard Space Flight Center (GSFC), Greenbelt, MD 20771, USA.

F.M Finkbeiner is with Sigma Space Corp. / Hexagon US Federal, 4600 Forbes Blvd., Lanham, MD 20706, USA and NASA Goddard Space Flight Center (GSFC), Greenbelt, MD 20771, USA.

J.Y. Ha is with SB Microsystems, 806 Cromwell Park Dr, Glen Burnie, MD 21061, USA and NASA Goddard Space Flight Center (GSFC), Greenbelt, MD 20771, USA.

S. Hull is a NASA Postdoctoral Program Fellow, NASA Goddard Space Flight Center, Greenbelt, MD 20771

S. Yoon is with Science Systems and Applications, Inc. (SSAI) 10210 Greenbelt Rd, Lanham, MD 20706

S.R. Bandler, J.A. Chervenak, R.L. Kelley, C.A. Kilbourne, F.S. Porter, S.J. Smith, and E.J. Wassell are with NASA Goddard Space Flight Center (GSFC), Greenbelt, MD 20771, USA

with an energy resolution of $2.5\,\mathrm{eV}$ at X-ray energies up to $7\,\mathrm{keV}$. The Mo/Au TES microcalorimeters for this mission have been developed over many years at NASA Goddard Space Flight Center. Recently, in close collaboration with National Institute of Standards and Technology, it was shown that the baseline TES design is capable of meeting X-IFU requirements using 32 row TDM in a demonstration of $> 200$ pixels in a 1000 pixel array [2]. Building upon this successful demonstration, our collaboration has continued to seek to improve the TES performance to create margin on the current requirements.

One area for potential refinement of the TES design is in the rise and fall-time of the X-ray pulse. In the current TES design there is margin to increase the fall-time of the pulse by $\sim 25\%$ and still meet count-rate requirements. By increasing the pulse rise-time, the slew-rate in the X-ray pulse, or the maximum time-derivative of the TES current $I$, will also be reduced. With a reduced slew-rate at the maximum X-ray energy, the mutual inductance of the first-stage SQUID readout may be increased, and this could (a) allow a reduction in the energy resolution degradation as a result of multiplexing with the current requirement of 34 rows, or (b) allow an increase in the multiplexing factor above 34 rows while maintaining current energy resolution performance [3].

A second area of potential improvement of the TES design is in the sensitivity of the X-ray response to external magnetic field. While the current baseline TES design meets the X-IFU requirements, there is little margin. The sensitivity of the TES to magnetic fields, both constant and time-varying, is important for determining the energy resolution, the uniformity of response of the TES array to X-rays, and the ability to calibrate and correct the energy gain-scale of this response [4], [5].

The current baseline design for X-IFU is a square TES with side length of $50\,\mu\mathrm{m}$. In this report, we discuss results of an exploration of changes to the TES dimensions as one avenue to improve overall TES performance for X-IFU. We have studied TES's with length ranging from $75\,\mu\mathrm{m}$ to $50\,\mu\mathrm{m}$ and width ranging from $50\,\mu\mathrm{m}$ to $15\,\mu\mathrm{m}$. We discuss how these changes to the TES dimensions affect the key parameters of the superconducting transition, the thermal conductance of the TES to the thermal bath, the slew-rate, energy resolution, and magnetic field sensitivity.

## II. METHODS

Figure 1 shows a generalized schematic diagram of the TES pixel design used in this study with length $L$ and width

$W$, which will be referred to in the following as an $L$ x $W$ TES. We have studied TES devices on two different detector
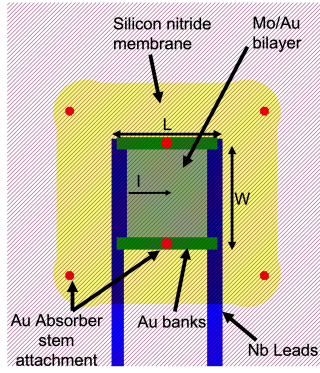


Fig. 1. Schematic diagram of TES design under study viewed from above with the Bi/Au absorber removed for clarity. $I$ indicates the TES current direction.

chips from two independently fabricated wafers. The Mo/Au bilayer in wafer 1 was $41.5/223$ nm thick with sheet resistance $R_\square = 18.5\,\mathrm{m\Omega/\square}$ and intrinsic bilayer transition temperature $T_{ci} \sim 88\,\mathrm{mK}$. The Mo/Au bilayer in wafer 2 was $46/257$ nm thick with $R_\square = 11.6\,\mathrm{m\Omega/\square}$ and intrinsic bilayer $T_{ci} \sim 80\,\mathrm{mK}$. Each TES also has a Bi/Au absorber mounted on the absorber stem attachments that is not shown in the diagram for clarity. The square absorbers had a side length of $\sim 269\,\mu\mathrm{m}$ and the Bi/Au bilayer had a typical thickness of $3/1.5\,\mu\mathrm{m}$. The TES was situated on a $0.5\,\mu\mathrm{m}$ thick silicon nitride membrane and had additional gold banks down the edge of the TES parallel to the current direction. The absorber stem attachments on the silicon nitride membrane were gold with a diameter of $4\,\mu\mathrm{m}$.

Below, we show results from measurement of the TES current $I$ as function of the bias circuit voltage $V$ to determine the TES resistance $R$ as function of TES temperature $T$, and the thermal conductance from the TES to the thermal bath $G_{bath}$. Through the use of complex impedance measurements we also show the transition parameters $\alpha = \frac{T}{R}\frac{\partial R}{\partial T}\big|_I$ and $\beta = \frac{I}{R}\frac{\partial R}{\partial I}\big|_T$. More details of the TES design, measurement circuit, and measurement techniques are given in [4], [6]–[8].

## III. RESULTS

### A. Transition Properties and Thermal Conductance

We begin by discussing the basic transition properties of the different devices we have studied. Figure 2 shows $R(T)$ for pixels with different TES lengths and widths. As discussed above, each of the measured wafers had a different $R_\square$ and $T_{ci}$ of the bilayer. This can be seen by the lower TES transition temperature $T_c$ and normal state resistance $R_n$ of the $50\times 50\,\mu\mathrm{m}$ devices from wafer 2 compared with wafer 1. As the TES becomes longer or narrower, $R_n$ increases as expected from the increased aspect ratio. $T_c$ decreases as the TES becomes longer because of the reduced proximity effect from the Nb leads, and as the TES becomes narrower because of the increased lateral inverse proximity effect from the Au banks down the edge of the TES. These effects have been discussed in detail elsewhere [9]–[11]. Note that the $T_c$ in the $50\,\mu\mathrm{m}$ x

$22.5\,\mu\mathrm{m}$ and $50\,\mu\mathrm{m}$ x $15\,\mu\mathrm{m}$ devices was too low to warrant comprehensive study in this wafer beyond $R(T)$ and $G_{bath}$.
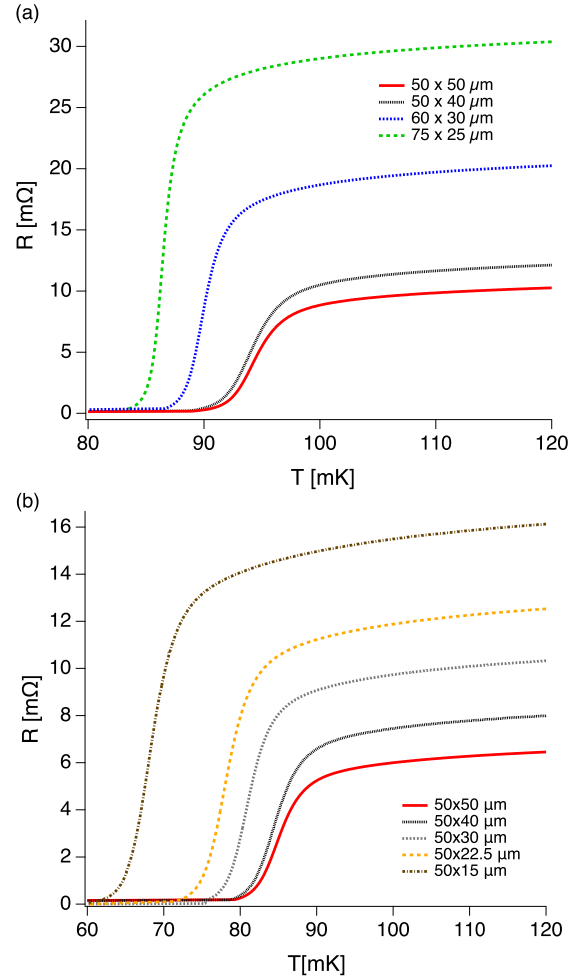


Fig. 2. TES resistance as a function of TES temperature for different TES designs on (a) wafer 1 and (b) wafer 2. Calculated from measurement of TES current as a function of applied voltage at $T_{bath} = 55\,\mathrm{mK}$, and measured $G_{bath}$ for each device.

The thermal conductance $G_{bath}$ for each TES from the two wafers is shown in Fig. 3 as a function of the TES perimeter. This shows $G_{bath}$ scales approximately linearly with the perimeter of the TES and the Au stems in contact with the silicon nitride membrane. This linear dependence of $G_{bath}$ on TES perimeter is in agreement with previous observations [11]–[13] and is expected when the thermal conductance is dominated by ballistic phonon transport in the membrane, as is the case here.

Figure 4 shows the transition parameters $\alpha$ and $\beta$ as a function of the bias point $R/R_n$ for a selection of the devices on each wafer. This shows a monotonic decrease in $\alpha$ and $\beta$ as a function of $R/R_n$. We also observe that as the TES length increases there is significant increase in $\alpha$ and decrease in $\beta$ for a given bias point. These results are consistent with previous observations that the ratio of $\alpha/\beta$ increases as the TES is made longer [7], [14]. For devices with L=$50\,\mu\mathrm{m}$ and varying width, the change in $\alpha$ and $\beta$ is less pronounced and is likely insignificant. There is currently no complete theory to
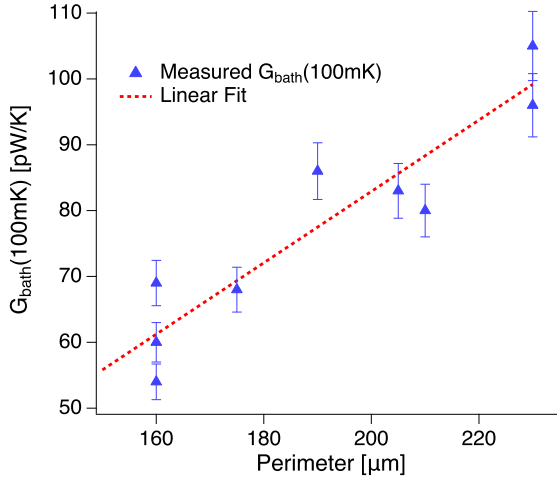
Fig. 3. Thermal conductance $G_{bath}$ of TES to the thermal bath as a function of perimeter of TES plus perimeter of base of Au absorber stems in contact with silicon nitride membrane. Note that the effective length of TES is calculated as $(L-10\,\mu m)$ in the perimeter calculation to account for the region of overlap between Nb leads and TES which does not contribute to phonon emitting perimeter.

describe the exact dependence of $\alpha$ and $\beta$ on TES size, $R_n$, and $T_c$. Here we observe an interesting difference between the transition parameters observed in identical device designs in the two different wafers, with $\alpha$ significantly lower and $\beta$ significantly higher in the devices from wafer 2. The reason for this change is not yet understood. One possibility is that the parameters are sensitive to $R_\square$ of the bilayer, which is significantly lower in wafer 2, and therefore sensitive to the current distribution across the TES and within the normal metal banks. However, more data will be needed to confirm this. The difference in $T_{ci}$ may also be important.

### B. Slew-Rate

Figure 5a shows the slew-rate, or maximum in the time-derivative of the TES current response, during a 6 keV X-ray event for different TES designs in this study. This is then compared to the measured response of a baseline pixel with the $50\,\mu m$ x $50\,\mu m$ TES design that was used in the latest demonstrations of TES performance for X-IFU [2] and is used here as a reference pixel. This shows that the measured slew-rate in the $75\,\mu m$ x $25\,\mu m$ and $60\,\mu m$ x $30\,\mu m$ TES designs is significantly higher than observed in the baseline pixel. However, the slew-rate in the $50\,\mu m$ x $30\,\mu m$ design is significantly lower.

The comparison of the slew-rates for different TES sizes is complicated by the variations in $T_c$, $R_n$ and the ratio of the circuit inductance to the critical inductance $L/L_{crit}$. Without an accurate model of these highly non-linear devices a direct renormalization is not possible. Instead, we must take an approximate renormalization using the linear small signal single-body model [6], [7]. To do this, for each design we have taken the predicted slew-rate $S$ in the small signal model using the measured parameters of $\alpha, \beta, R, T_c, L, G_{bath}$, shunt resistance $R_{shunt}$, as well as the heat capacity that is approximately constant for all these devices. We then calculate
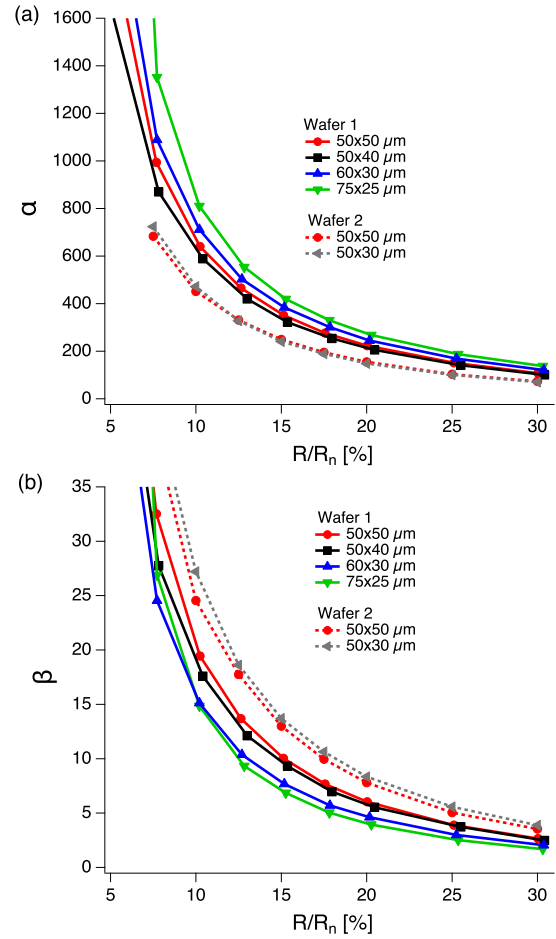


Fig. 4. (a) $\alpha = (T/R)\,\partial R/\partial T\,|_I$ and (b) $\beta = (I/R)\,\partial R/\partial I|_T$ as a function of TES resistance $R$ as fraction of normal state resistance $R_n$.

the predicted slew-rate for that design $S_N$ in the small signal model if $L/L_{crit}$, $T_c$, $R_{shunt}$, and $R$ were equal to that of the baseline reference pixel, while all other parameters are held at their measured values. The measured slew-rate is then multiplied by this factor of $S_N/S$ to give the normalized slew-rate for each device. This normalized slew-rate is plotted in Fig. 5b. The trends shown in Fig 5a are broadly unchanged by this normalization. The slew-rate of the $75\,\mu m$ x $25\,\mu m$ and $60\,\mu m$ x $30\,\mu m$ designs are significantly higher than the $50\,\mu m$ x $50\,\mu m$ designs. In the small signal limit the slew-rate is expected to be proportional to $G_{bath}^{3/2}$ and therefore one might have expected the slew-rate to be reduced in the $60\,\mu m$ x $30\,\mu m$ TES. However, both the higher $\alpha$ and lower $\beta$ in this TES increase the slew-rate, and this dominates over the effect of the reduced $G_{bath}$. In the $50\,\mu m$ x $30\,\mu m$ design the normalized slew-rate is reduced by 31% compared to the $50\,\mu m$ x $50\,\mu m$ device from the same wafer. This is in reasonable agreement with the 35% reduction in slew-rate expected from the $\sim25\%$ reduction in $G_{bath}$ shown in Fig. 3 as the perimeter is reduced from $230\,\mu m$ to $190\,\mu m$. Note that the measured slew-rate in the $50\,\mu m$ x $50\,\mu m$ TES in wafer 2 is significantly lower than the baseline reference pixel. This is likely a consequence of the low $\alpha$ and high $\beta$ in wafer 2, but warrants further investigation.
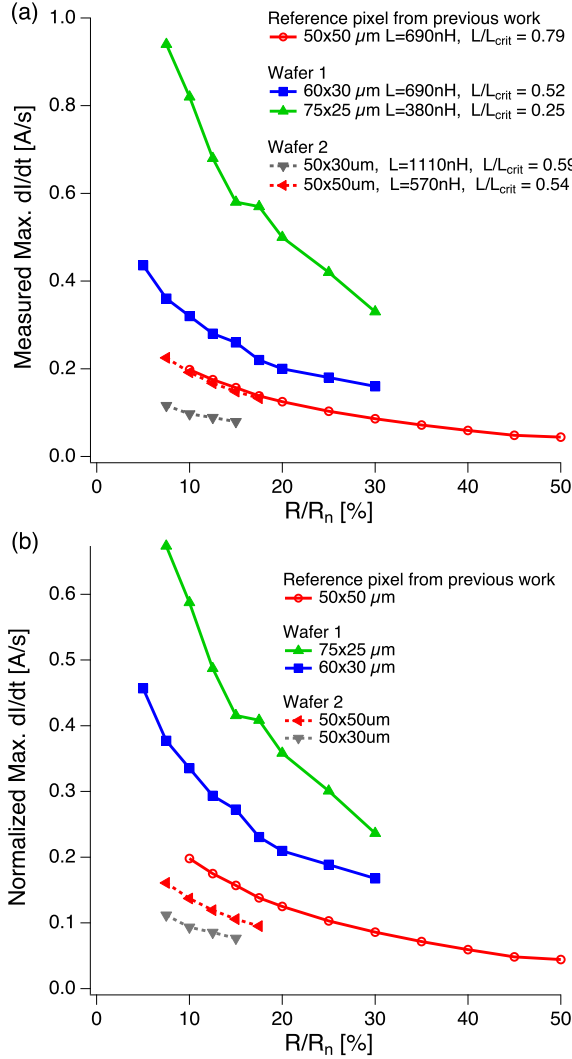
Fig. 5. (a) Maximum in time-derivative of TES current $dI/dt$ during a MnK$\alpha$ X-ray pulse as a function of TES resistance $R/R_n$ for several TES designs in this study compared to a reference pixel used in previous performance demonstrations [2]. (b) This measured slew-rate normalized to the $T_c$, $R_n$, $R_{shunt}$, and $L/L_{crit}$ of the reference pixel. The normalization scale-factor for each TES design was calculated as the fractional change in slew-rate in the small signal single-body model for the given pixel parameters.

## C. Energy Resolution

Table I shows the measured energy resolution $\Delta E$ for the MnK$\alpha$ complex on several different designs of TES from the two fabricated wafers and the reference baseline pixel. Comparison of the energy resolution of these devices is complicated by the variation in $T_c$ and $L/L_{crit}$. If all pixel parameters are constant then energy resolution is expected to scale with $T_c^{3/2}$ in the small signal limit. However, it has been shown that these devices are highly non-linear and deviate significantly from small signal predictions. In general, one manifestation of this is a strong dependence of integrated noise equivalent power on $L/L_{crit}$. The energy resolution, however, is found to depend more weakly on $L/L_{crit}$ as long as $L/L_{crit} < 1$. Therefore, while detailed comparison is not possible, we can draw broad conclusions from the results of Table I. In Wafer 1, the energy resolution in the $75\,\mu m$ x $25\,\mu m$ and $60\,\mu m$ x

$30\,\mu m$ devices is slightly better than in the $50\,\mu m$ x $50\,\mu m$. However, when scaled for the reduced $T_c$ the difference in normalized energy resolution $\Delta E_N$ is within the measurement uncertainty. The intrinsic bilayer $T_{ci}$ in wafer 2 is lower than in wafer 1, and therefore we might have expected an improved energy resolution in this wafer. However, as shown in Fig. 4, the $\alpha$ is significantly lower and $\beta$ significantly higher in the devices from wafer 2 and this even negates any improvement from the lower $T_c$.

TABLE I
ENERGY RESOLUTION AT $6\,keV$
FOR DIFFERENT TES DESIGNS AT $R/R_n = 10\%$

| TES size L[μm]xW[μm] | $L/L_{crit}$ | $T_c$ [mK] | $\Delta E$ [eV] | $\Delta E_N$ [a] [eV] |
|---|---|---|---|---|
| **Ref. Pixel** [b] | | | | |
| 50 x 50 | 0.65 | 93 | 1.9 ± 0.1 | 1.9 ± 0.1 |
| **Wafer 1** | | | | |
| 50 x 50 | 0.1 | 94 | 2.16 ± 0.13 | 2.13 ± 0.13 |
| 60 x 30 | 0.52 | 91 | 1.77 ± 0.12 | 1.83 ± 0.12 |
| 75 x 25 | 0.25 | 87 | 1.61 ± 0.20 | 1.78 ± 0.2 |
| **Wafer 2** | | | | |
| 50 x 50 | 0.59 | 86 | 2.04 ± 0.11 | 2.29 ± 0.11 |
| 50 x 30 | 0.54 | 82 | 1.91 ± 0.11 | 2.30 ± 0.11 |

[a] Estimated energy resolution when normalized to $T_c \sim 93\,mK$ of baseline reference pixel.
[b] Reported in [2].

## D. Magnetic Field Sensitivity

It has been shown previously that TES devices are highly sensitive to an applied magnetic field $B$ perpendicular to the plane of the TES [4], [9], [10], [15]. This is a consequence of the TES acting as a Josephson weak-link and therefore the TES critical current $I_c$ forming a Fraunhofer-type pattern as function of magnetic field. This field dependence means that the current pulse-height from an X-ray event is dependent on magnetic field. For small changes in $B$ close to zero, one expects $dI_c/dB$ to reduce linearly as the area of the TES is reduced and therefore the period of the Fraunhofer pattern of $I_c(B)$ increases, assuming all other parameters are constant, including $G_{bath}$. However, in the devices tested here there are two additional contributions that affect $dI_c/dB$. First, the current in the TES creates its own self-magnetic field which is dependent on $R_n$ and $G_{bath}$ [4]. Second, the current distribution across the width of the TES affects the width of the central maximum of the Fraunhofer pattern [15], [16]. As the TES is made narrower, the lateral inverse proximity effect from the normal metal banks at the edge of the TES increasingly leads to a higher current density at the center of the TES compared with the edge. This broadens the central maximum and therefore further reduces $dI_c/dB$. This field dependence of $I_c$ impacts $I(B)$ for constant voltage bias. This is demonstrated in Fig. 6, which shows $I(B)$ for the $50\,\mu m$ x $50\,\mu m$ and $50\,\mu m$ x $30\,\mu m$ TES designs from wafer 2 when a constant voltage bias is applied to give $R/R_n = 10\%$ at $B = 0$. Note the larger $dI/dB$ in the $50\,\mu m$ x $50\,\mu m$ device and the additional features in the curve.

The variation in $I(B)$ means that the current pulse-height from an X-ray event is dependent on magnetic field. Figure 7
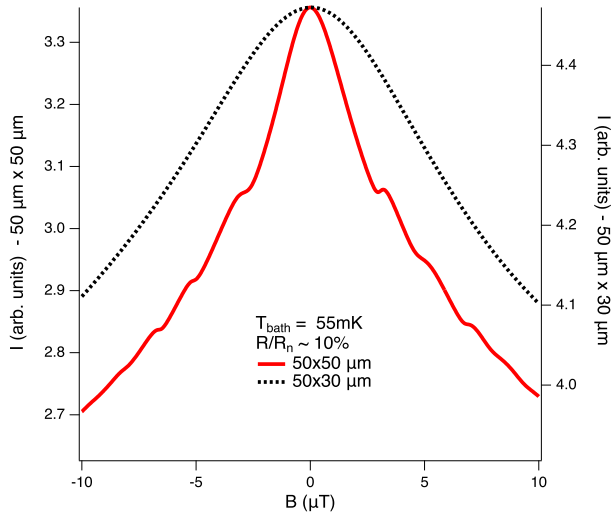
Fig. 6. TES current $I$ as a function of magnetic field $B$ for two TES designs from wafer 2. Thermal bath temperature $T_{bath}$ was at $55\,\mathrm{mK}$ and TES's were biased with a constant voltage such that $R/R_n = 10\%$ at $B = 0$.
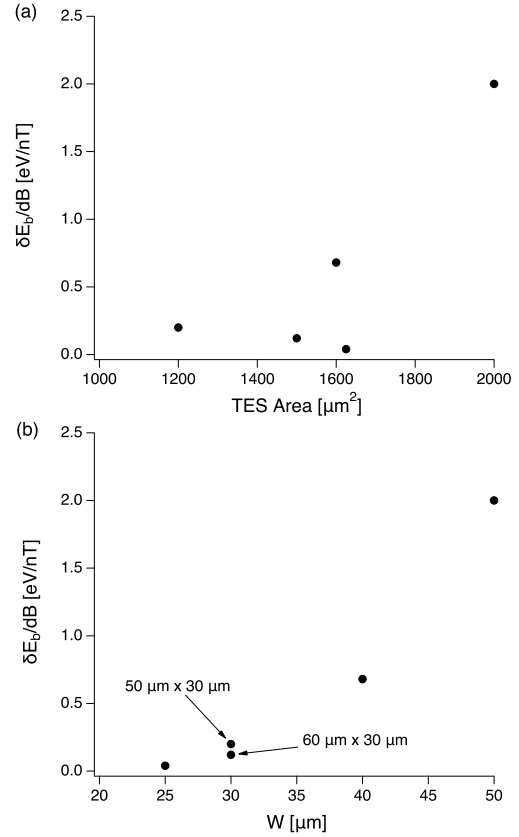


Fig. 7. The energy gain-scale of the TES changes by $\delta E_b$ as a function of small changes in magnetic field . The derivative of this change in gain-scale with respect to magnetic field $B$ is shown for $6\,\mathrm{keV}$ X-rays as a function of (a) TES area and (b) TES width. Note that the TES area is calculated as $W(L - 10\,\mu\mathrm{m})$ to account for the region of overlap between the Nb leads and the TES.

shows this magnetic field dependence calculated as a change in the energy gain-scale $\delta E_B$, after optimal filtering, divided by the change in magnetic field B in units of $\mathrm{eV\,nT^{-1}}$ for each TES design. Figure 7a shows a weak correlation of the reduction of $\delta E_B/dB$ with reducing TES area. Figure 7b shows the much stronger correlation of $\delta E_B/dB$ with TES width.

## IV. DISCUSSION

The results presented above demonstrate several key findings as small changes are made to the TES dimensions from the baseline $50\,\mu\mathrm{m}$ x $50\,\mu\mathrm{m}$ design. First, $R_n$, $T_c$ and $G_{bath}$ vary as expected as a function TES dimensions and Mo/Au bilayer properties. The behavior of the transition properties, $\alpha$ and $\beta$, are more subtle. In general, we observe an increase in $\alpha/\beta$ as the TES length is increased, and little change when TES width is decreased for a fixed length, but there also appears to be a significant variation in $\alpha$ and $\beta$ between the two wafers studied. This may be a consequence of the different $R_\square$ and $T_{ci}$ in the two wafers, but as yet there is no theory to accurately predict this behavior, and therefore these effects require further study.

The slew-rate data presented indicate that although $G_{bath}$ is reduced in the $60\,\mu\mathrm{m}$ x $30\,\mu\mathrm{m}$ TES compared to the $50\,\mu\mathrm{m}$ x $50\,\mu\mathrm{m}$, as expected, this does not lead to an overall reduction in slew-rate because of the change in transition parameters $\alpha$ and $\beta$. This means this design, and the $75\,\mu\mathrm{m}$ x $25\,\mu\mathrm{m}$ TES, are most likely not good candidates to try to improve on the performance on X-IFU at the current multiplexing factor, or a suitable route for an increase in multiplexing factor. The limited data presented in Table I also suggest that there is no significant improvement in the intrinsic energy resolution of these devices either. The $50\,\mu\mathrm{m}$ x $30\,\mu\mathrm{m}$ TES design, however, does offer a more promising route to improve on the current baseline pixel design. The $G_{bath}$ in this design is reduced from the $50\,\mu\mathrm{m}$ x $50\,\mu\mathrm{m}$ design, as expected, but in this case

the transition properties are very similar. This leads to a $\sim$ 31% reduction in slew-rate compared to the $50\,\mu\mathrm{m}$ x $50\,\mu\mathrm{m}$ design on the same chip, once normalized for differences in $T_c$, $R_n$ and $L/L_{crit}$. From initial measurements of the energy resolution of this design, it also appears that this improvement in slew-rate is achieved with no significant change to energy resolution.

Finally, measurements of the sensitivity of the TES energy gain-scale to magnetic field have shown that a significant improvement can be achieved by making the TES narrower. The improvement is larger than might be expected from a linear area scaling. This is likely a consequence of the self-magnetic field and current distribution also changing as the TES width is reduced. This means that any of the designs studied here could be suitable options to reduce the magnetic-field sensitivity of the X-IFU pixels. In particular, the $50\,\mu\mathrm{m}$ x $30\,\mu\mathrm{m}$, which showed a reduction in slew-rate, showed a reduction of $\delta E_B/dB$ of a factor of $\sim 10$ compared with the $50\,\mu\mathrm{m}$ x $50\,\mu\mathrm{m}$ design on the same chip.

## V. CONCLUSION

The data presented above show that by reducing the TES size from $50\,\mu\mathrm{m}$ x $50\,\mu\mathrm{m}$ in the current baseline design for X-IFU to $50\,\mu\mathrm{m}$ x $30\,\mu\mathrm{m}$ there is a significant reduction in the

maximum of the time-derivative of the TES current response to a $6\,\mathrm{keV}$ X-ray because of the reduced thermal conduction from the TES to the thermal bath. This reduced slew-rate could allow X-IFU to be operated with the currently baselined multiplexing factor, and potentially improved energy resolution, or allow the use of a higher multiplexing factor. The change in TES width to $30\,\mu\mathrm{m}$ also reduces the magnetic field sensitivity of the energy gain-scale to $\delta E_B/dB \sim 0.2\,\mathrm{eV\,nT^{-1}}$, which may give margin on this important requirement for X-IFU.

In the future we must demonstrate that a uniform array of these pixels, with optimized Mo/Au bilayer parameters and added circuit inductance, is able to achieve improved performance under time division multiplexing while also continuing to meet all of the other requirements of X-IFU.

## REFERENCES

[1] D. Barret *et al.*, "The Athena X-ray Integral Field Unit (X-IFU)", *Proc. SPIE 9905*, Space Telescopes and Instrumentation 2016: Ultraviolet to Gamma Ray, 99052F (17 August 2016); https://doi.org/10.1117/12.2232432

[2] S. J. Smith *et al.*, "Performance of a broad-band, high-resolution, transition-edge sensor spectrometer for X-ray astrophysics" *IEEE Trans. Appl. Supercond.*, vol. 31, no. 5, pp. 1-6, Aug. 2021, Art no. 2100806, https://doi.org/10.1109/TASC.2021.3061918.

[3] Doriese, W.B. *et al.* "Optimization of the TES-bias Circuit for a Multiplexed Microcalorimeter Array", *J. Low Temp. Phys.* 167, 595-601 (2012). https://doi.org/10.1007/s10909-012-0509-7

[4] S. J. Smith *et al.*, "Implications of weak-link behavior on the performance of Mo/Au bilayer transition-edge sensors", *J. App, Phys.*, 114, 074513 (2013) https://doi.org/10.1063/1.4818917

[5] S. J. Smith *et al.*, "Uniformity of Kilo-Pixel Arrays of Transition-Edge Sensors for X-ray Astronomy", *IEEE Trans. Appl. Supercond.*, vol. 25, no. 3, pp. 1-5, June 2015, Art no. 2100505, doi: 10.1109/TASC.2014.2369352.

[6] K. D. Irwin and G. C. Hilton, "Cryogenic Particle Detection", Chapter 3, Vol. 99 (Springer, 2005)

[7] N. A. Wakeham *et al.*, "Thermal fluctuation noise in Mo/Au superconducting transition-edge sensor microcalorimeters", *J. App. Phys.*, 125, 164503 (2019) https://doi.org/10.1063/1.5086045

[8] M. A. Lindeman *et al.*, "Impedance measurements and modeling of a transition-edge-sensor calorimeter", *Rev. Sci. Instrum* 75, 1283 (2004), DOI:10.1063/1.1711144.

[9] J. Sadleir, S. J. Smith, S. R. Bandler, J. A. Chervenak, and J. R. Clem, *Phys. Rev. Lett.*, "Longitudinal Proximity Effects in Superconducting Transition-Edge Sensors", 104, 047003, (2010), https://doi.org/10.1103/PhysRevLett.104.047003

[10] J. Sadleir *et al.*, "Proximity effects and nonequilibrium superconductivity in transition-edge sensors", *Phys. Rev. B*, 84, 184502, (2011), https://doi.org/10.1103/PhysRevB.84.184502

[11] M. de Wit *et al.*, "High aspect ratio transition edge sensors for x-ray spectrometry", *J. Appl. Phys.*, 128, 224501, (2020), https://doi.org/10.1063/5.0029669

[12] H. F. C. Hoevers *et al.*, "Radiative ballistic phonon transport in silicon-nitride membranes at low temperatures", *Appl. Phys. Lett.* 86, 251903 (2005) https://doi.org/10.1063/1.1949269

[13] E. Taralli *et al.*, "Performance and uniformity of a kilo-pixel array of Ti/Au transition-edge sensor microcalorimeters", *Rev. Sci. Instrum.* 92, 023101 (2021) https://doi.org/10.1063/5.0027750

[14] Miniussi, A.R. *et al.*, "Performance of an X-ray microcalorimeter with a $240\,\mu\mathrm{m}$ absorber and a $50\,\mu\mathrm{m}$ TES bilayer". J Low Temp Phys 193, 337-343 (2018). https://doi.org/10.1007/s10909-018-1974-4

[15] Wakeham, N.A. *et al.*, "Effects of normal metal features on superconducting transition-edge sensors". J Low Temp Phys 193, 231-240 (2018). https://doi.org/10.1007/s10909-018-1898-z

[16] J. E. Sadleir, "Superconducting transition-edge sensor physics", Ph.D. Thesis, University of Illinois, (2010)